Caveolin-1 regulates context-dependent signaling and survival in Ewing sarcoma.

Dagan Segal[1], Xiaoyu Wang[2], Hanieh Mazloom-Farisbaf[1], Felix Y. Zhou[1], Divya Rajendran[1], , Erin Butler[3,4], Bingying Chen[1], Bo-Jui Chang[1], Khushi Ahuja[1], Averi Perny[1], Kushal Bhatt[1], Dana Kim Reed[1], Diego H. Castrillon[5], Jeon Lee[1], Elise Jeffery[6], Lei Wang[1,8], Khai Nguyen[9], Noelle S. Williams[2], Stephen X. Skapek[3,4**], Satwik Rajaram[1], Reto Fiolka[1,7], Khuloud Jaqaman[1,9], Gary Hon[1,8], James F. Amatruda[10,11*], Gaudenz Danuser[1*]

1. *Lyda Hill Department of Bioinformatics, UT Southwestern Medical Center, Dallas, TX*
2. *Department of Biochemistry, UT Southwestern Medical Center, Dallas, TX*
3. *Department of Pediatrics, Division of Hematology/Oncology, University of Texas Southwestern Medical Center, Dallas, TX, USA.*
4. *Harold C. Simmons Comprehensive Cancer Center, University of Texas Southwestern Medical Center, Dallas, TX, USA.*
5. *Department of Pathology, UT Southwestern Medical Center, Dallas, TX*
6. *Children's Medical Center Research Institute, UT Southwestern Medical Center, Dallas, TX*
7. *Department of Cell Biology, UT Southwestern Medical Center, Dallas, TX*
8. *Cecil H. and Ida Green Center for Reproductive Biology Sciences, UT Southwestern Medical Center, Dallas, TX*
9. *Department of Biophysics, UT Southwestern Medical Center, Dallas, TX*
10. *Cancer and Blood Disease Institute, Children's Hospital Los Angeles, Los Angeles, CA*
11. *Departments of Pediatrics, Medicine and Cancer Biology, Keck School of Medicine, University of Southern California, Los Angeles, CA*

**co-corresponding authors*

***current affiliation is Department of Pediatrics, Duke University School of Medicine, Durham, NC*

ABSTRACT:

Plasticity is a hallmark function of cancer cells, yet the mechanisms that enable dynamic switching between survival states remain incompletely understood. Here, we identify Caveolin-1, a membrane-domain scaffolding protein, as a context-dependent regulator of survival signaling in Ewing sarcoma (EwS). Single-cell analyses reveal a distinct subpopulation of EwS cells marked by high CD99 and elevated Caveolin-1 expression. These CD99^{High} cells exhibit unique morphology, transcriptional programs, and markedly enhanced survival both under

chemotherapeutic challenge and *in vivo.* Importantly, CD99^{High} and CD99^{Low} states are reversible, providing EwS cells with a flexible route to survival-oriented plasticity. Mechanistically, we show that Caveolin-1 in CD99^{High} cells orchestrates PI3K/AKT survival signaling by modulating the spatial organization of PI3K activity on the plasma membrane. We propose that the CD99^{High} state establishes a Caveolin-1-driven signaling architecture that supports survival through mechanisms distinct from those used by CD99^{Low} cells. These findings uncover a dynamic state transition in EwS cells and position Caveolin-1 as a key driver of context-specific survival signaling.

INTRODUCTION

Cellular adaptation is a hallmark of cancer, driving intratumoral heterogeneity and contributing to tumor growth, metastasis, and therapeutic resistance [1]. Across many cancer types and under varying stresses, phenotypically distinct yet genetically similar subpopulations with different growth and metastatic capabilities have been identified [2]. However, the underlying mechanisms often remain poorly understood. This gap in knowledge is especially critical in pediatric cancers, which tend to exhibit a low mutational burden beyond a single driver, despite variability in patient outcome [3, 4]. In this work, we focus on Ewing sarcoma (EwS) as a prototype of pediatric cancer. EwS is the second most common malignant bone tumor occurring in children and young adults, characterized by a single chromosomal translocation leading to the formation of a chimeric fusion oncogene transcription factor, most commonly EWSR1::FLI1 [5, 6]. While much research has focused on EWSR1::FLI1 as the putative driver of distinct EwS cell states [7, 8], more recent works have identified EwS cell states with distinct gene signatures not classically associated with EWS::FLI1 gene expression [9-11]. In either case, the signaling mechanisms that drive segregation of cell states remain largely unknown.

One possible mechanism driving distinct cell states could be through regulation of signaling pathways on the plasma membrane, which integrates signals from the extracellular environment through targeted, localized signaling cascades. Differential organization of modified lipids or activated receptors on the cell surface into subcellular domains can affect downstream signaling[12, 13]. A prominent example of such domains can be observed in caveolae, cave-like membrane invaginations that are rich in cholesterol and sphingolipids[14] and have roles in signal transduction [15-20]. Caveolae are considered specialized lipid domains, with effects on membrane fluidity and lipid species composition[21, 22]. These structures are prominently found in a subset of

cell types, such as adipocytes and muscle cells, and have been implicated in many cancers[23, 24], including Ewing Sarcoma [25, 26]. Several studies have demonstrated that perturbation of caveolae through mechanical means [27-29] or perturbations of the key structural protein Caveolin-1 affect canonical cancer signaling pathways, such as Src[16, 19, 20], Erk1/2[26, 30], and PI3K/Akt activation [31, 32]. Some of these studies have demonstrated differential subcellular organization of specific signaling molecules upon loss of caveolae [30, 33]. However, whether and how caveolae-based organization of signaling contributes to cellular plasticity in development and disease remains unclear.

In this study, we identified a distinct EwS cell population characterized by reduced proliferation but enhanced viability both *in vivo* and in response to chemotherapeutic treatment. We refer to this population as CD99^{Hi} cells, defined by their elevated expression of the surface marker CD99. CD99^{Hi} cells display high endogenous Caveolin-1 levels, are enriched in caveolae, and depend on Caveolin-1 for their survival advantage. Mechanistically, we show that loss of Caveolin-1 prevents CD99^{Hi} cells from recruiting active PI3K to the plasma membrane, thereby impairing activation of the PI3K/AKT survival pathway. Together, these findings reveal a mechanism by which EwS cells can adapt survival signaling in a context-dependent manner.

RESULTS

High CD99 marks a distinct Ewing Sarcoma cell state.

Nongenetic heterogeneity in cancer cells has increasingly been recognized as a critical driver of aggressive disease progression and treatment resistance [1, 2]. To study heterogeneity in EwS cell populations, we first used single cell transcriptomics to identify cell surface markers that would readily enable isolation of distinct subpopulations for further downstream characterization (Figure 1A). Given that cell surface receptors are sensitive to cleavage through standard enzymatic passaging techniques and inspired by classic studies in mesenchymal stem cells [34-36], we reasoned that cells passaged through mechanical means rather than enzymatic cleavage would enable the discovery of distinct subpopulations of cells, as well as preserve surface receptors intact as targets for flow cytometry. Applied to the EwS cell line TC71, single-cell transcriptomic analysis uncovered a cluster of cells with a unique transcriptional profile, characterized by enrichment of extracellular matrix (ECM) structural constituents (Figure S1A,B).

We next profiled the relative expression of transcripts of surface receptors between these two populations. Of 348 previously validated targets[37], seven surface receptors were enriched in

the distinct cluster (Figure 1B). Among those was the glycoprotein CD99 (Figure 1B,C), a commonly used biomarker for EwS[38]. Based on their distinct CD99 expression levels, we designate these population as $CD99^{Hi}$ and $CD99^{Lo}$ cells. A $CD99^{Hi}$ cluster was also similarly observed in EWS1, a patient derived xenograft (PDX) line (Figure 1D). The EWS1 $CD99^{Hi}$ cluster was similarly enriched for ECM structural constituents (Figure S1B), suggesting conservation of the $CD99^{Hi}$ cellular phenotype in EwS. Through flow cytometric analysis in TC71 cells, we uncovered a bimodality of CD99 distributions, representing intermediate and high levels of CD99 protein expression (Fig 1E). Notably, the detection of the $CD99^{Hi}$ state depended on mechanical passaging and vanished under conventional enzymatic dissociation mechanisms (i.e. Trypsin; Figure S1C), suggesting that this EwS subpopulation may have been overlooked in previous studies. The $CD99^{Hi}$ state appears to be reversible, since $CD99^{Hi}$ cells that were isolated and subsequently grown for several passages again displayed a bimodal distribution of CD99 expression upon flow cytometric analysis (Fig 1F).

$CD99^{Hi}$ cells display differences in morphology, gene expression, and survival *in situ.*

We subsequently utilized CD99 as a flow cytometry marker to isolate and characterize the two cell states. Strikingly, the two subpopulations exhibited distinct morphological phenotypes (Figure 2A, Figure S2A). The $CD99^{Hi}$ cells were flat with thick actin bundles, whereas the $CD99^{Lo}$ cells were rounded, clustered, and enriched in filopodia.

We next examined the broader features of the $CD99^{Hi}$ population. Bulk transcriptomic analysis revealed that TC71 $CD99^{Hi}$ cells were enriched for gene ontology terms related to neural differentiation compared to $CD99^{Lo}$ cells (Figure 2B). Growth and viability assays showed no differences between $CD99^{Hi}$ and $CD99^{Lo}$ cells when grown in adherent flasks (Fig S2B). However, $CD99^{Hi}$ cells displayed decreased growth capabilities in soft environments *in vitro* (Fig S2C). To test whether $CD99^{Hi}$ cells show tumor growth or survival differences *in vivo,* we performed intratibial xenografts of isolated Luciferase-expressing $CD99^{Hi}$ or $CD99^{Lo}$ TC71 cells, respectively, in immunocompromised mice. $CD99^{Hi}$ cells showed dramatically lower tumor burden compared to $CD99^{Lo}$ cells (Figure 2C, S3A). A computerized tomography scan also revealed that bony destruction, a phenomenon frequently found in EwS tumors and described as moth-eaten appearance of the bone[30], was decreased in xenograft performed with $CD99^{Hi}$ cells (Figure 2D, S3B).

To study these apparent differences in tumor growth more deeply we turned to an analysis of histological sections. Tumor cells were identified morphologically through H&E staining and by

CD99 immunohistochemistry (Figure 2E, S3C). Differences in CD99 expression appeared to be maintained between CD99^{Hi} and CD99^{Lo} tumors (Figure 2E, Figure S3C), suggesting distinct phenotypic cell states were sustained *in situ.* Strikingly, most tumor growth of CD99^{Lo} cells occurs through the local invasion of surrounding muscle, while both cell populations grow masses of limited size within the medullary cavity of the bone (Figure 2F, S3C). To test for survival and proliferation differences, we combined the TUNEL assay with immunostaining for the proliferation marker Ki67 in serial histological slides. For clusters of comparable size within the medullary cavity, the CD99^{Lo} cells show comparable cell proliferation but strikingly more cell death compared to CD99^{Hi} cells (Figure 2E). Differences in cell death appear to hold true for local muscle invasions as well (Figure S3D). To determine whether morphological differences were also preserved *in situ*, we performed morphological feature classification on tumor nuclei in H&E-stained histological sections. CD99^{Hi} and CD99^{Lo} cells occupied distinct regions in shape feature space (Figure S3E). Notably, CD99^{Hi} cells exhibited site-specific differences in shape features, whereas CD99^{Lo} cells showed considerable overlap in feature space across seeding sites, suggesting that CD99^{Hi} cells may have a greater capacity to adapt to diverse microenvironments.

We wondered whether the putative adaptivity of CD99^{Hi} cells also confers greater resilience to drug challenges. To test this, we grew a mixed population of CD99^{Hi} and CD99^{Lo} cells in the presence or absence of Doxorubicin (DOXO, 0.5uM), which serves as part of frontline therapy of EwS[38, 39]. By flow cytometry we found that DOXO treatment causes higher cell death in the CD99^{Lo} cell population (Figure 2G). Closer examination of the surviving cells revealed a significant enrichment of CD99^{Hi} cells upon drug treatment, suggesting these cells have a survival advantage under these stress conditions (Figure 2H).

To test distinct behavior between CD99^{Hi} and CD99^{Lo} tumors at the single cell level, we performed cancer cell xenografts in the hindbrain ventricle (HBV) of 2-day old zebrafish, which is permissive to high-resolution imaging[40]. Using cell morphology as a functional readout of cell state, we first examined whether distinctions in cell state were maintained in this *in vivo* environment. For this purpose, we injected a cell mixture consisting of 90% unsorted TC71 cells expressing the nuclear marker H2B-GFP, and 10% CD99^{Hi} or CD99^{Lo} cells expressing the actin tag Ftractin-mRuby2 (Figure 3A-B). Following fixation in 4% paraformaldehyde (PFA) and 3D imaging of the zebrafish larvae at 1-day post-injection, we computationally extracted the cell volumes of individual CD99^{Hi} or CD99^{Lo} cells for morphotype analysis, as previously

described[40]. CD99^{Hi} cells displayed distinctly more irregular shapes than CD99^{Lo} cells (Figure 3C-D), suggesting that these EwS cells maintain the morphological differences *in vivo*.

We next used xenografts in zebrafish to test differences in survival between the two cell populations in the HBV. For this purpose, we injected CD99^{Hi} or CD99^{Lo} cells expressing F-Tractin-mRuby2 into the HBV. Through chemical fixation at 2 days post-injection followed by apoptotic TUNEL staining, we observed significantly reduced cell death in CD99^{Hi} cells compared to CD99^{Lo} cells (Figure 3E-F), akin to the situation in the tibial xenografts in mice. Taken together, the results presented thus far suggest that the CD99^{Hi} population acquires a transcriptionally and functionally distinct cell state, potentially with survival advantages in certain tissues.

Caveolin-1 emerges as a molecular signature of CD99^{Hi} State.

Next, we sought to identify the potential molecular mediators that would drive functionally distinct states. Given that expression levels of the oncogene EWSR1::FLI1 have previously been implicated as a major regulator of plasticity in Ewing Sarcoma[7, 8] and CD99 itself is a transcriptional target of EWSR1::FLI1[41], we first tested whether differences in oncogene levels differed in the CD99^{Hi} state. While differences in CD99 expression between CD99^{Hi} and CD99^{Lo} cells were confirmed by western blot, EWSR1::FLI1 protein expression levels remained consistent between the two groups (Figure S4A). We therefore sought to look more broadly to identify potential molecular signatures that could drive the functionally distinct states of CD99^{Hi} and CD99^{Lo} cells. Several initial lines of evidence converged around the scaffolding protein Caveolin-1 (Cav-1) as a potential regulator of CD99^{Hi} cells. First, Cav-1 expression was highly enriched at the transcript level in the TC71 CD99^{Hi} cluster by single-cell transcriptomics (Figure 4A). Second, through a functional proteomics screen based on a Reverse Phase Protein Array (RPPA), we observed Cav-1 as the most differentially enriched protein in TC71 CD99^{Hi} cells compared to CD99^{Lo} cells (Figure 4B). Third, ultrastructure analysis by electron microscopy revealed an abundance of caveolae, Cav-1-driven cholesterol-rich membrane invaginations[14], in CD99^{Hi} cells but not in CD99^{Lo} cells (Figure 4C). Similarly, colocalization analysis of Cav-1 with the structural caveolar component PTRF/Cavin-1[43] through immunofluorescence revealed high colocalization in CD99^{Hi} but not in CD99^{Lo} cells, further validating the enrichment of caveolae in CD99^{Hi} cells (Figure S4B-C). Quantitative analysis of diffusion dynamics of Cav-1 puncta showed slower diffusion in CD99^{Hi} cells (Figure S4D), another signature of stable caveolar structures[44]. Cav-1 is upregulated in metastases across several cancer types[45], including

EwS[25, 26], and has been implicated in diverse processes, including cell signaling, membrane trafficking, and stress response, making it a promising candidate for further investigation.

To investigate whether Cav-1 drives the CD99^{Hi} state, we established a tetracycline (TET)-inducible shRNA knockdown system targeting Cav-1, combined with an RFP reporter, in TC71 cells. Strikingly, Cav-1 knockdown markedly reduced the density of membrane invaginations in CD99^{Hi} cells, demonstrating that changes in Cav-1 expression directly regulate the formation of caveolae (Figures 4C). However, inducible Cav-1 knockdown had no effect on CD99 expression (Figure S4E). Using a similar approach to target CD99 expression, we found that CD99 knockdown reduced Cav-1 expression in CD99^{Lo} cells but had no effect in CD99^{Hi} cells (Figure S4F). These findings suggest that CD99 can function as an upstream positive regulator of Cav-1, but this regulatory relationship is bypassed once cells adopt the CD99^{Hi} state.

To determine whether the chemotherapy resistance of CD99^{Hi} cells is Cav-1 dependent, we assessed the viability of mixed CD99^{Hi}/ CD99^{Lo} cell population in response to acute treatment with 10 μM DOXO, with or without Cav-1 knockdown. While Cav-1 knockdown did not confer an overall survival advantage under drug treatment (Figure S4G), detailed analysis of the surviving CD99+ population revealed a critical dependency on Cav-1. In cells with endogenous Cav-1 expression, DOXO treatment enriched for CD99^{Hi} cells (Figures 2H, 4D). However, this enrichment was abolished following Cav-1 knockdown, resulting in comparable proportions of CD99^{Hi} and CD99^{Lo} cells (Figure 4D). These findings demonstrate that Cav-1 is required for the survival advantage of CD99^{Hi} cells under stress from chemotherapy, suggesting a Cav-1-dependent survival signaling pathway in this cellular state.

Caveolin-1 regulates PI3K/AKT signaling in CD99^{Hi} Cells

The change in viability upon drug treatment prompted us to examine changes in survival signaling pathways. By RPPA we noted in CD99^{Hi} cells an enrichment of Receptor Tyrosine Kinases that have been associated with the activation of the phosphatidylinositol 3-kinase (PI3K)/Akt survival signaling pathway, namely EphA2, VEGFR, c-Kit, and Axl (Figure 4B, Table S1)[46-49]. Indeed, western blot analysis confirmed increased active Akt at baseline Cav-1 in CD99^{Hi} cells both in TC71 (Figure 5A) and RD-ES (Figure S5) lines when compared to their CD99^{Lo} counter parts. Knockdown of Cav-1 in TC71 cells drastically reduced phosphorylated Akt levels in CD99^{Hi} cells (Figure 5A), suggesting a dependence on Caveolin-1 for their Akt signaling.

The downstream effects of PI3K/Akt signaling on diverse cell functions rely on recruitment of the active molecule to the cell surface[50]. We therefore applied a high-resolution imaging approach to measure the levels and organization of PI3K activity at the surfaces of individual TC71 cells. We employed a GFP-tagged Akt-PH construct as a reporter of the local concentration of PI3K-activated lipid products[51, 52] in CD99^{Hi} cells, CD99^{Lo} cells, and CD99^{Hi} cells with Cav-1 KD, seeded on glass coverslips (Figure 5B). Both CD99^{Hi} and CD99^{Lo} cells showed comparable membrane enrichment of active PI3K (Figure 5B-C). Strikingly, Cav-1 knockdown markedly reduced membrane-localized PI3K activity in CD99^{Hi} cells. Control experiments using a lipophilic membrane dye showed no significant differences between conditions (Figure S5B-C), indicating that the observed changes are specific to PI3K signaling. These findings suggest that Cav-1 modulates PI3K/Akt signaling in CD99^{Hi} cells by regulating PI3K activation or recruitment at the plasma membrane.

DISCUSSION

In this study, we uncover a subpopulation of EwS cells characterized by distinctions in transcriptional signature, cell morphology, and growth *in vivo.* These cells can be identified and isolated through flow cytometry based on their high expression of the cell surface receptor CD99, a glycoprotein often used as a diagnostic marker in EwS[53]. Functional characterization of CD99^{Hi} cells demonstrates a survival advantage in certain tissues *in vivo* and in response to a chemotherapeutic drug. We determine the protein Cav-1 as a key regulator of this context-dependent cell survival in CD99^{Hi} cells through regulation of PI3K signaling.

Cell state heterogeneity is a major factor in driving drug resistance and metastasis in cancer [1], creating an urgent clinical need to better understand the underlying mechanisms. In EwS, as in many pediatric cancers[4], mutational tumor burden beyond a single driver mutation is low, suggesting that non-genetic mechanisms are a primary factor in modulating cell state heterogeneity. Several previous works have identified variability in expression levels of the oncogene EWSR1::FLI1 or its transcriptional signature as a driver of variable EwS cell states [8, 37, 41, 54], largely through experimental knockdown approaches. Notably, both CD99 and Cav-1 are direct targets of EWS:FLI1[55]. However, the differences between CD99^{Hi} and CD99^{Lo} cells described in this work appear to be agnostic to the oncogene level. While CD99 served as a convenient marker of the distinct cell states, our results suggest that CD99 expression does not drive the particular functions associated with the CD99^{Hi} state. Rather, CD99^{Hi} cells show

increased neural differentiation, as well as survival advantages and repressed tumor growth *in vivo,* phenotypes which have been associated with reduced CD99 expression in other works[53, 56]. While CD99 serves as a clinical prognostic marker of EwS[5], endogenous heterogeneity in its expression with functional consequences has not previously been described. The emergence of the CD99^{Hi} state only upon non-enzymatic passaging may explain why this subpopulation of cells was overlooked in past studies. Our findings therefore define a previously uncharacterized EwS cell state with distinct functional behavior, expanding our understanding of non-genetic heterogeneity in this tumor.

We chose to pursue Cav-1 as a potential driver of distinct cell states in EwS cells due to the high differential expression levels of Cav-1 and striking difference in presence of Cav-1-driven caveolae in the CD99^{Hi} cells. Depletion of Cav-1 affected activation of downstream signaling pathways, and the ability of cells to survive under drug challenge. Since CD99^{Lo} cells do not display caveolae, have different growth and survival phenotypes *in vitro* and *in situ*, and show distinct organization and expression of downstream signaling pathways, we conjecture that this population of cells relies on alternative, Cav-1 independent mechanisms to regulate its cell survival.

Cav-1 is known to regulate key cellular signaling pathways, such as Src- family kinases, receptor tyrosine kinases, and RAS signaling[16, 19, 20, 20, 31, 32]. Whether these effects are through direct binding of Cav-1 to components of the signaling pathway, or through alternate mechanisms, remains unclear. One possibility is that Cav-1 can indirectly influence downstream signaling through changes in the composition and biophysical properties of the plasma membrane[21, 22]. This is evidenced by the protein's ability to selectively recruit specific lipids, such as cholesterol and PtdIns(4,5)P2, to caveolae [33], as well as its role in RAS nanoclustering[30]. Some studies have demonstrated flattening of caveolae and subsequent release of Cav-1 in response to mechanical stress[29, 57], suggesting that these structures can also serve as passive buffers of cell surface tension by acting as membrane reservoirs. Previous studies have described context-dependent and often contradictory effects of Cav-1 on the PI3K/Akt survival signaling pathway, with evidence for both activation[31, 32, 42] and inhibition[58-60], but the underlying molecular mechanisms remain unclear. In our system, CD99^{Hi} cells localized active PI3K to the plasma membrane to a similar degree as CD99^{Lo} cells, yet showed markedly higher level of downstream phospho-AKT, suggesting more efficient transduction of PI3K-activated lipid products to AKT signaling. Both enhanced AKT signaling and recruitment of active PI3K to the cell surface were dependent on Cav-1. Together, these findings support a

model in which Cav-1 alters plasma membrane composition to enhance PI3K recruitment and AKT activation in CD99^{Hi} cells (Figure 5D). Reduced Cav-1 expression in CD99^{Hi} cells drives altered membrane properties, resulting in impaired propagation of active PI3K signaling. Future studies will explore the extrinsic cues that promote enrichment of Cav-1-dependent CD99^{Hi} states in EwS and the biophysical properties of the plasma membrane that underlie their enhanced signaling capacity, with the goal of uncovering new vulnerabilities in EwS tumor biology.

METHODS

Cell culture and cell line generation

Cells were cultured at 5% CO2 and 21% O2. TC71 and RDES cells were cultured using RPMI (Gibco) supplemented with 10% FBS and 1% antibiotic antimycotic. For enzymatically passaged cells, cells were treated with 0.05% Trypsin-EDTA (GIBCO 15400054) up to 5 minutes. For mechanical passaging, cells were grown in T125 cell-culture treated flasks (Corning 430825), and iteratively washed with PBS by tapping of flask to detach cells. Cells were then reseeded in the same flask for 2-6 weeks until mixed cell morphologies of the CD99^{HI} and CD99^{LO} cell states were readily observed.

TC71 Cav1, EF1, and CD99 shRNA lines cells were generated using the pZIP shRNA Promoter selection kit (https://www.transomic.com/cms/home.aspx). shRNA knockdown was induced by continuous 1 µg/ml tetracycline in cell culture, and shRNA knockdown induction was verified by RFP reporter expression and Western blotting.

Fluorescent constructs were introduced into TC71 cells using the pLVX lentiviral system (Clontech) and selected using antibiotic resistance to either puromycin or neomycin. The GFP-FTractin and mRuby2-FTractin constructs contain residues 9–52 of the enzyme IPTKA30 fused to eGFP or mRuby2, respectively. pLenti6-H2B-GFP was acquired from Addgene (generated by Fuchs lab, New York University, plasmid # 25999; Addgene*).* The GFP-AktPH construct was obtained from the laboratory of Jason Haugh (North Carolina State University, Raleigh NC)[61] and cloned into the pLVX-IRES-puro vector (Clontech).

Endogenously tagged TC71 Cav-1-mClover was generated through CRISPR-based knock-in strategy. Briefly, two guides were generated using CRISPOR[62] (gRNA1: GCATCCCGATGGCACTCATC and gRNA2: GACCCACTCTTTGAAGCTGT), and were cloned into plasmid pSpCas9(BB)-2A-Puro (Feng Zhang lab, plasmid # 62988, Addgene). The donor

vector was generated using plasmid pMA-Tia1L which was a gift from Tilmann Bürckstümmer [63].

RPPA

Functional Proteomics Reverse Phase Protein Array (RPPA) was performed by the RPPA core at MD Anderson Cancer Center. Cellular proteins were denatured in a 1% SDS + 2-mercaptoethanol buffer solution and diluted in five 2- fold serial dilutions in dilution lysis buffer. Serially diluted lysates were arrayed on nitrocellulose-coated slides (Grace Bio-Labs) by the Quanterix (Aushon) 2470 Arrayer (Quanterix Corporation). A total of 5808 spots were arrayed on each slide including spots corresponding to serially diluted (1) standard lysates, and (2) positive and negative controls prepared from mixed cell lysates or dilution buffer, respectively. Each slide was probed with a validated primary antibody plus a biotin-conjugated secondary antibody. Antibody validation for RPPA is described in the RPPA Core website: https://www.mdanderson.org/research/research-resources/core-facilities/functional-proteomics-rppacore/antibody-information-and-protocols.html. Signal detection was amplified using an Agilent GenPoint staining platform (Agilent Technologies) and visualized by DAB colorimetric reaction. The slides were scanned (Huron TissueScope, Huron Digital Pathology) and quantified using customized software (Array-Pro Analyzer, Media Cybernetics) to generate spot intensity. Relative protein level for each sample was determined by RPPA SPACE (developed by MD Anderson Department of Bioinformatics and Computational Biology, https://bioinformatics.mdanderson.org/public-software/rppaspace/)[64] by which each dilution curve was fitted with a logistic model. RPPA SPACE fits a single curve using all the samples (i.e., dilution series) on a slide with the signal intensity as the response variable and the dilution steps as the independent variable. The fitted curve is plotted with the signal intensities, both observed and fitted, on the y-axis and the log2 concentration of proteins on the x-axis for diagnostic purposes. The protein concentrations of each set of slides were then normalized for protein loading. Correction factor was calculated by (1) median-centering across samples of all antibody experiments; and (2) median-centering across antibodies for each sample. Results were then normalized across RPPA sets by replicates-based normalization as described[65]. Details of the RPPA platform as performed by the RPPA Core are described in[66].

Transcriptomics

For single cell RNA-seq, RDES and TC71 cell lines were dissociated in Tryp-LE express enzyme (GIBCO), resuspended in 0.04% BSA in PBS, and passed through a 70um filter before diluting to 1000 cells/uL. NCH- EWS1 and SJEWS001321_X1 PDX lines were kindly provided by Peter Houghton (University of Texas Health Sciences center San Antonio), and St. Jude Children's Research Hospital Childhood Solid Tumor Network (SJEWS001321_X1), respectively. For PDXs, tumor chunks >5 grams were dissociated using Trypsin and Collagenase, treated with a combination of DNAse and Magnesium Chloride to dissolve DNA, and passed through a 40um filter and treated with a Red Blood Cell lysis buffer before resuspending in 0.04% BSA in PBS and diluting to 1000 cells/uL. Samples were processed as in 10× Genomics Chromium 3' V3.1 with Cell Multiplexing kit and pooled together evenly for a final concentration of 1500 cells/μL in 0.04% BSA in PBS. Single-cell RNA-seq libraries were prepared using 10× Genomics Chromium 3′ V3.1 kit, following the standard protocol.

Single-cell RNA sequencing (scRNA-seq) data were generated for three samples: NCH-NCH-EWS1 PDX, SJEWS001321_X1 PDX, and TC71 cell line using the 10x Genomics platform. The data were processed using the Cell Ranger pipeline (version 6.0.0) to generate gene-barcode matrices, which were subsequently analyzed in Seurat (version 5.0.2). For each sample, raw count matrices, barcodes, and feature files were loaded into Seurat to create individual Seurat objects. Quality control was meticulously performed to exclude cells with extreme total RNA counts (nCount_RNA) and detected features (nFeature_RNA), with thresholds set based on the 5th and 95th percentiles for RNA counts, and the 10th and 90th percentiles for detected features. Additionally, cells with high mitochondrial content, indicative of potential cell stress or apoptosis, were filtered out by excluding cells with mitochondrial transcript percentages exceeding 15%. Data normalization was conducted using the "LogNormalize" method with a scale factor of 10,000, and highly variable features were identified using the "vst" method with 2,000 features selected for downstream analysis. Principal component analysis (PCA) was applied for dimensionality reduction, followed by clustering using the Louvain algorithm and visualization using Uniform Manifold Approximation and Projection (UMAP). Cell cycle scoring was performed by classifying cells into G1, S, and G2/M phases based on established markers. Specifically, cells in the G1 phase were subsetted for more focused analysis, ensuring that cell cycle effects were minimized in the downstream analyses. Gene Set Enrichment Analysis (GSEA) was conducted on the differentially expressed genes, utilizing pathways relevant to the EWSR1::FLI1 fusion as described by Siligan and Torchia. Furthermore, marker gene expression, such as CD99, was profiled across the different

clusters, and volcano plots were generated to highlight significant differentially expressed genes.

Flow Cytometry

For flow cytometry, TC71 cells were dissociated in Tryp-LE express enzyme, resuspended in 5% FBS in PBS, and passed through a 70um filter before diluting to 1X10^6 cells/mL. For live cell staining of CD99, cell suspension was incubated with mouse anti-human PE-CD99 antibody (BD Pharmingen 555689, 1:6). For shRNA expressing cell lines expressing RFP, cell suspension was incubated with rabbit monoclonal CD99 antibody (Abcam EPR3096 1:50) followed by secondary anti-rabbit antibody conjugated to AlexaFlour 405 (Abcam ab175652, 1:1000). For viability staining in Figure S4D, cells were additionally stained with 1:1000 Live-Dead fixable Far-Red stain (ThermoFisher L34973) prior to flow cytometry. Samples were analyzed or sorted based on CD99 detected fluorophore intensity using BD FACSAria Zelda (BD BioSciences) flow cytometers. Flow cytometry plots were visualized using FloJo Software (BD Bioscences).

Western Blots

Primary antibodies used for western blotting were anti-CD99 (Abcam; EPR3096), Fli1 (Abcam; ab133485), Tubulin, Cav-1 (Cell Signaling; #3267), pAKT (Cell Signaling; #4060), AKT (Cell Signaling; #2920), Histone H3 (Cell Signaling: #9715), Phospho-PI3K (Invitrogen, #17387), PI3K (Cell Signaling, #42925).

Zebrafish husbandry and xenografts

Danio rerio were maintained in an Aquaneering aquatics facility according to industry standards. Vertebrate animal work was carried out by protocols approved by the institutional animal care and use committee at UT Southwestern, an Association for Assessment and Accreditation of Laboratory Animal Care accredited institution. Wild Indian Karyotype (WIK) wild-type lines used were obtained from the Zebrafish International Resource Center (zebrafish.org).

For xenografts of TC71-Ftractin-mRuby2 cells, cells were sorted for *CD99 High* and *CD99 Low* populations, then expanded prior to injection. Preparation of cell mixture consisted of 90% mRuby2-Ftractin labeled cells and 10% unsorted H2B-GFP labeled cells, or 100% mRuby2-Ftractin labeled cells, as indicated. Cell mixtures (2×10^6 cells) were run through a 70-μm cell strainer and resuspended in 5% FBS in PBS mixture for optimal cell viability.

Zebrafish embryos were collected, dechorionated, and treated with 0.1 mM phenylthiourea starting at 24 h post fertilization to prevent pigmentation. Xenografts were generated by microinjection of cell mixture into zebrafish larvae (2 days post fertilization [dpf]) with glass capillary needles into HBV. For each cell xenograft group, cells were injected into 3-aminobenzoic acid ethyl ester (Tricaine)–anesthetized embryos. Injected zebrafish larvae were incubated for 1–2 d in 34°C before imaging.

For immunostaining of zebrafish larvae, anesthetized embryos were fixed in 4% paraformaldehyde/1XPBS for 2 h in scintillation vials, rinsed in PBS +0.5% Tween, and stored in PBS up to 2 wk. Immunostaining was carried out as previously described (Miller et al., 2015). Primary antibodies were rabbit anti-GFP (ab290; Abcam) and mouse anti-Phospho-Histone H3 (9706S; Cell Signaling). TUNEL assay was performed using the ApopTag Green In-Situ Apoptosis Detection Kit (Millipore).

Mouse xenografts

All experiments involving animals were reviewed, approved, and monitored for compliance by the UT Southwestern Institutional Animal Care and Use Committee.

Lenti-luciferase-P2A-Neo was acquired from Addgene (Vakoc lab, Cold Spring Harbor Laboratory, plasmid: #105621; Addgene), and introduced into TC71 cells, which were subsequently sorted for *CD99 High and CD99 Low* populations and expanded prior to xenografts. Maintenance of isolated cell states was validated by distinct cell morphology in cell culture. Orthotopic intratibial xenografts were performed in NOD *scid* gamma chain knockout (NSG) mice, following a previously established protocol[67]. Briefly, the top of the right tibia was punctured with a 25 gauge needle, followed by injection of $5x10^5$ cells suspended in 5ul media into the medullar cavity of the bone using a 27 gauge needle from a tuberculine syringe (Cat 26040, Exelint, Int. Co, Redondo Beach, CA) coupled to a 0.1 ml Hamilton syringe (Cat 8001, Hamilton Co, Reno, NV).

Functional imaging to monitor tumor growth in live mice was performed using the IVIS Spectrum System (PerkinElmer). At each imaging session, 80 µL of a Luciferin working solution (40 mg/mL in PBS without calcium or magnesium) was administered. Mice were imaged at 0, 7, 14, 21, 28, 35, and 42 days post-injection. Regions of interest (ROIs) around the injection site were manually delineated for quantitative analysis of total flux [photons/second]. Luciferin signals

observed in the liver were excluded from the analysis. At the end of the experiment, tumor-bearing Grossly trimmed tibia samples and their encapsulating musculature and non-tumor bearing counter-parts from the same mouse were harvested for further evaluation.

For micro-Computer Tomography (microCT) scans, formaline-fixed samples were scanned using a Scanco Medical µCT 35. Tibias were scanned at an isotropic voxel size of 3.5µm, with peak tube voltage of 55 kV and current of 0.145 mA (µCT 35; Scanco). A Gaussian filter (s = 0.8) with a limited, finite filter support of one was used to suppress noise. Mineralized bone was segmented from air and soft tissues by intensity thresholding. Scanco Medical software was used to determine bone volume.

Mouse tumor histology

Grossly trimmed tibia samples and their encapsulating musculature from each condition were formalin-fixed, decalcified 14% ethylenediaminetetraacetic acid disodium salt dihydrate in paraffin-embedded, and sectioned at 4 µm thickness. Serial sections were used for Hematoxylin and Eosin staining (H&E), immunohistochemistry (IHC), immunofluorescence (IF), and TUNEL assay. All histology samples were evaluated by an expert pathologist.

Confirmation of proliferating cells and cell death were assessed by IF of Ki-67 (Leica, Cat# KI67-MM1-L-CE, 1:300) and DeadEnd Fluorometric TUNEL assay (Promega; Cat #: G3250), respectively, and counterstained with propidium iodide. IHC of CD99 staining was done with rabbit monoclonal CD99 antibody (Abcam EPR3096 1:50), using the SignalStain Boost IHC detection reagent (Cell Signaling Cat #8114), as directed.

All slides were digitally scanned on a Nanozoomer S60 (Hamamatsu) or Axioscan 7 (Zeiss) systems. Measurements of area were made through manual annotations of ROIs on images using NDP.view2 (Hamamatsu).

Electron Microscopy

For each treatment, duplicate cell monolayers were grown on MatTek dishes. After an initial wash with PBS, the monolayers were washed with 0.1 M sodium cacodylate and then with 2.5% (v/v) glutaraldehyde in 0.1M sodium cacodylate buffer. After fixation, the monolayers were rinsed five times in 0.1 M sodium cacodylate buffer, then were post-fixed in 1% osmium tetroxide and 0.8 % K3[Fe(CN)6] in 0.1 M sodium cacodylate buffer for 1 hour at 4 degrees C. Cells were rinsed with water and en bloc stained with 2% aqueous uranyl acetate overnight at 4 degrees C. After five rinses with water, specimens were dehydrated with increasing

concentration of ethanol at 4 degrees C, infiltrated with Embed-812 resin and polymerized in a 60°C oven overnight. Embed-812 disc was removed from MatTek plastic housing by submerging the dish in liquid nitrogen. Two discs were sandwiched together side to cell side by putting a drop of Embed-812 and polymerized in a 60°C oven overnight. Sandwiched discs were sectioned perpendicular with a diamond knife (Diatome) on a Leica Ultracut UCT (7) ultramicrotome (Leica Microsystems) and collected onto copper grids, post stained with 2% Uranyl acetate in water and lead citrate. TEM images were acquired on a JEOL-1400 Plus transmission electron microscope equipped with a LaB6 source operated at 120 kV using an AMT-BioSprint 16M CCD camera.

Imaging

Light-sheet fluorescence microscopes were used to image the zebrafish larvae within a custom-made mount. Fixed zebrafish larvae were embedded in 1% low-melting agarose into sonicated, ethanol-washed fluorinated ethylene propylene tubes (Zeus, HS 029EXP/ .018 REC). In this case, the tube is held by a custom-made mount, which allows 3D translation and rotation in our light-sheet microscopes. A conventional mSPIM[68] was used as previously described[40]. Briefly, a 40× NA 0.8 water-dipping objective (CFI Apo NIR 40XW; Nikon Instruments) was used for detection, at room temperature in PBS. A 200-mm focal length tube lens (58-520; Edmund Optics) that formed the image on an sCMOS camera (ORCA-Flash4.0; Hamamatsu Photonics). These conditions provide a resolution of 380 nm laterally and about 1.4 μm axially. A 10× NA 0.28 objective (M Plan Apo 10×, 378-803-3; Mitutoyo) was used for light-sheet illumination. The thickness and the length of the light-sheet were controlled by a variable slit (VA100C; Thorlabs) placed at the conjugate plane of the back focal plane of the illumination objective.

For live imaging on glass, F-Tractin-GFP and GFP-AktPH cells were mounted on a glass-bottom 35 mm cover dish (MatTek). GFP-AktPH cells were stimulated with Insulin Growth Factor (IGF) prior to imaging. IGF stimulation was done using 1nM Human IGF-1 recombinant protein (Peprotech) for 15 minutes, following 4 hours serum starvation. In some cases, GFP-AktPH cells were additionally labeled with a lipophilic membrane dye (CellBrite Steady Membrane Dye, biotium, 1:1000) immediately prior to imaging. Mounted cells were subsequently imaged using a custom-built Oblique Plane Microscope (OPM), as previously described[69]. Briefly, a tilted light sheet was launched after a primary objective (25x NA 1.1, Nikon MRD77220) to illuminate the cells in a glass-bottom dish; the fluorescence was collected by the same objective and formed the image on the camera after passing through the optical train with the magnification of around 43.3. By scanning the light sheet using Galvo mirrors in

the optical train, we can rapidly acquire the 3D image of the cells without any mechanical movement of either sample or objective. Also, using a single objective for both illumination and fluorescence collection frees the whole sample space above the objective and makes the system compatible with the standard sample mounting methods. The resolution of the system across the extended FOV was around 0.39, 0.43, and 1.22 μm in the x, y, and z directions, respectively.

To image dynamics of Cav-1 puncta, TC71 Cav1-mClover cells were imaged on a SoRA spinning disc confocal microscope (Nikon) at 100X magnification, NA1.45, 200ms exposure, at 2 second time intervals. PTRF and Cav1-mClover localization was imaged on LSM780 scanning confocal microscope (Zeiss) at 40X magnification, NA1.4.

Image Analysis

For quantification of Cav-1 puncta dynamics, particle detection and tracking were performed using u-track (version 2.4; https://github.com/DanuserLab/u-track)[70]. The detection algorithm used was Gaussian-mixture model fitting, using default parameters. The mean localization precision per movie was 8.5-12.1 nm. The resulting detections were then tracked over time, using default tracking parameters. The detection and tracking results were verified using visual inspection as well as using the performance diagnostics included in u-track. Tracks lasting for at least 10 frames were then analyzed to obtain each track's diffusion coefficient from its frame to frame displacements[71, 72].

For 3D morphology classifications in zebrafish, images were segmented using the previously established 3D morphology pipeline[73] to segment cell volumes and calculate local membrane curvature from single cell images. For the segmentation process, we smoothed the deconvoluted images with a 3D Gaussian kernel (σ = 3 pixels) and applied a gamma correction (Υ = 0.7), then employed an Otsu threshold, followed by a 3D grayscale flood-fill operation to fill possible holes. The binary images of all cells were visually inspected for segmentation artifacts. Miss-segmented cells were excluded from the data set. Aspect Ratio was calculated on segmented volumes using "regionprops3" in MATLAB. 3D rendering were generated using ChimeraX[74].

To quantify differences in tissue morphology between $CD99^{Hi}$ and $CD99^{Lo}$ cells xenografted in mice, we compared various aspects of nuclear morphology in Hematoxylin and Eosin (H&E) stained histological slides. First, tumor regions to be analyzed were manually annotated using QuPath[75] on tissue images from 3 slides in each experimental group, scanned at 40X

magnification (~0.25 microns/pixel). Second, nuclei in these regions were segmented using the PanNuke version of the HoverNet model as implemented in the TIAToolbox[76]. Third, these images were downsampled to 20X magnification and their color intensities we normalized using the Macenko algorithm[77] against a single (randomly selected) reference slide. Finally, we extracted 37 morphological features relating to size, shape, color, and texture of each individual nucleus, as previously described[78]. Then for each annotated tumor region we randomly selected neighborhoods of 25 nuclei: the number of neighborhoods was proportional to the area of the region but capped at 500 neighborhoods. Each neighborhood was then represented by a feature vector of the median value of individual features across constituent cells, which were then pooled across slides, z-score normalized, and visualized using T-distributed Stochastic Neighbor Embedding (t-SNE) .

For analysis of active PI3K organization or membrane dye enrichment on the cell surface in 2D maximum intensity projection images, we segmented each cell and windowed its peripheral boundary. Each window was ≈ 2.88 μm x 2.88 μm. To window, we implemented the conformalized mean curvature flow deformation from the u-Unwrap3D framework[79] (https://github.com/DanuserLab/u-unwrap3D) into the 2D u-Unwrap framework[80] (https://github.com/DanuserLab/u-unwrap) to deform the 2D cell boundary, equipartitioned the cell boundary and grouped together the corresponding deformed points of each boundary partition. For intensity measurement, we measured the mean fluorescence signal within each window, and computed the ratio enrichment with respect to the mean fluorescence signal averaged over the whole cell area. To compare the intensity distribution shift across conditions using a single summary statistic we computed the 90th percentile of the mean window normalized intensity for each cell.

Plots and statistical tests were visualized and preformed using GraphPad Prism.

ACKNOWLEDGMENTS

We would like to thank UT Southwestern Whole Brain Microscopy Facility (grant award number 1S10OD032267-01 to Denise Ramirez), Flow Cytometry Core Facility, Histo Pathology Core Facility, and Quantitative Light Microscopy Core Facility (grant award number 1S10OD028630-01 to Katherine Luby-Phelps), for their contributions to this work.

Funding for this work in the Danuser, Fiolka, and Amatruda labs has been provided by the grant 1U54CA268072 (NCI). Some microscope development in the Fiolka lab has been supported by R33 CA235254 (National Cancer Institute). D. Segal acknowledges funding from European

Molecular Biology Organization Long-term Research Fellowship (ALTF 626-2018) and the grant K99 CA270285 (NCI). X. Wang and N.S. Williams acknowledge funding from the NCI (1U54CA231649) and institutional support from UTSW for the Preclinical Pharmacology Core. Funding in the Jaqaman lab is provided through R35 GM119619 (National Institute of General Medical Sciences) and the UT Southwestern Endowed Scholars program.

DECLARATION OF INTERESTS:

G.D. is member of the board of Glencoe Software, Inc. and an advisor for the Allen Institute of Cell Science. The authors declare no other competing interests.

1. Hanahan, D. & Weinberg, R.A. Hallmarks of cancer: the next generation. *Cell* **144**, 646-674 (2011).
2. Quintanal-Villalonga, A. *et al.* Lineage plasticity in cancer: a shared pathway of therapeutic resistance. *Nat Rev Clin Oncol* **17**, 360-371 (2020).
3. Grobner, S.N. *et al.* The landscape of genomic alterations across childhood cancers. *Nature* **555**, 321-327 (2018).
4. Crompton, B.D. *et al.* The genomic landscape of pediatric Ewing sarcoma. *Cancer Discov* **4**, 1326-1341 (2014).
5. Grunewald, T.G.P. *et al.* Ewing sarcoma. *Nat Rev Dis Primers* **4**, 5 (2018).
6. Delattre, O. *et al.* The Ewing family of tumors--a subgroup of small-round-cell tumors defined by specific chimeric transcripts. *N Engl J Med* **331**, 294-299 (1994).
7. Aynaud, M.M. *et al.* Transcriptional Programs Define Intratumoral Heterogeneity of Ewing Sarcoma at Single-Cell Resolution. *Cell Rep* **30**, 1767-1779 e1766 (2020).
8. Franzetti, G.A. *et al.* Cell-to-cell heterogeneity of EWSR1-FLI1 activity determines proliferation/migration choices in Ewing sarcoma cells. *Oncogene* **36**, 3505-3514 (2017).
9. Wrenn, E.D. *et al.* Cancer-Associated Fibroblast-Like Tumor Cells Remodel the Ewing Sarcoma Tumor Microenvironment. *Clin Cancer Res* **29**, 5140-5154 (2023).
10. Gao, Y. *et al.* ETV6 dependency in Ewing sarcoma by antagonism of EWS-FLI1-mediated enhancer activation. *Nat Cell Biol* **25**, 298-308 (2023).
11. Lu, D.Y. *et al.* The ETS transcription factor ETV6 constrains the transcriptional activity of EWS-FLI to promote Ewing sarcoma. *Nat Cell Biol* **25**, 285-297 (2023).
12. Bankaitis, V.A., Mousley, C.J. & Schaaf, G. The Sec14 superfamily and mechanisms for crosstalk between lipid metabolism and lipid signaling. *Trends Biochem Sci* **35**, 150-160 (2010).
13. Grecco, H.E., Schmick, M. & Bastiaens, P.I. Signaling from the living plasma membrane. *Cell* **144**, 897-909 (2011).
14. Anderson, R.G. The caveolae membrane system. *Annu Rev Biochem* **67**, 199-225 (1998).
15. Couet, J., Sargiacomo, M. & Lisanti, M.P. Interaction of a receptor tyrosine kinase, EGF-R, with caveolins. Caveolin binding negatively regulates tyrosine and serine/threonine kinase activities. *J Biol Chem* **272**, 30429-30438 (1997).
16. Couet, J., Li, S., Okamoto, T., Ikezu, T. & Lisanti, M.P. Identification of peptide and protein ligands for the caveolin-scaffolding domain. Implications for the interaction of caveolin with caveolae-associated proteins. *J Biol Chem* **272**, 6525-6533 (1997).
17. Garcia-Cardena, G. *et al.* Dissecting the interaction between nitric oxide synthase (NOS) and caveolin. Functional significance of the nos caveolin binding domain in vivo. *J Biol Chem* **272**, 25437-25440 (1997).
18. Galbiati, F. *et al.* Caveolin-1 expression inhibits Wnt/beta-catenin/Lef-1 signaling by recruiting beta-catenin to caveolae membrane domains. *J Biol Chem* **275**, 23368-23377 (2000).
19. Labrecque, L. *et al.* Src-mediated tyrosine phosphorylation of caveolin-1 induces its association with membrane type 1 matrix metalloproteinase. *J Biol Chem* **279**, 52132-52140 (2004).
20. Gottlieb-Abraham, E. *et al.* Src-mediated caveolin-1 phosphorylation affects the targeting of active Src to specific membrane sites. *Mol Biol Cell* **24**, 3881-3895 (2013).
21. Sohn, J., Lin, H., Fritch, M.R. & Tuan, R.S. Influence of cholesterol/caveolin-1/caveolae homeostasis on membrane properties and substrate adhesion characteristics of adult human mesenchymal stem cells. *Stem Cell Res Ther* **9**, 86 (2018).

22. Parton, R.G., Kozlov, M.M. & Ariotti, N. Caveolae and lipid sorting: Shaping the cellular response to stress. *J Cell Biol* **219** (2020).
23. Campos, A. *et al.* Cell Intrinsic and Extrinsic Mechanisms of Caveolin-1-Enhanced Metastasis. *Biomolecules* **9** (2019).
24. Nunez-Wehinger, S. *et al.* Caveolin-1 in cell migration and metastasis. *Curr Mol Med* **14**, 255-274 (2014).
25. Sainz-Jaspeado, M. *et al.* Caveolin-1 modulates the ability of Ewing's sarcoma to metastasize. *Mol Cancer Res* **8**, 1489-1500 (2010).
26. Lagares-Tena, L. *et al.* Caveolin-1 promotes Ewing sarcoma metastasis regulating MMP-9 expression through MAPK/ERK pathway. *Oncotarget* **7**, 56889-56903 (2016).
27. Yeh, Y.C., Ling, J.Y., Chen, W.C., Lin, H.H. & Tang, M.J. Mechanotransduction of matrix stiffness in regulation of focal adhesion size and number: reciprocal regulation of caveolin-1 and beta1 integrin. *Sci Rep* **7**, 15008 (2017).
28. Goetz, J.G. *et al.* Biomechanical remodeling of the microenvironment by stromal caveolin-1 favors tumor invasion and metastasis. *Cell* **146**, 148-163 (2011).
29. Sinha, B. *et al.* Cells respond to mechanical stress by rapid disassembly of caveolae. *Cell* **144**, 402-413 (2011).
30. Ariotti, N. *et al.* Caveolae regulate the nanoscale organization of the plasma membrane to remotely control Ras signaling. *J Cell Biol* **204**, 777-792 (2014).
31. Zhang, B. *et al.* Caveolin-1 phosphorylation is required for stretch-induced EGFR and Akt activation in mesangial cells. *Cell Signal* **19**, 1690-1700 (2007).
32. Yang, H. *et al.* Mechanosensitive caveolin-1 activation-induced PI3K/Akt/mTOR signaling pathway promotes breast cancer motility, invadopodia formation and metastasis in vivo. *Oncotarget* **7**, 16227-16247 (2016).
33. Zhou, Y. *et al.* Caveolin-1 and cavin1 act synergistically to generate a unique lipid environment in caveolae. *J Cell Biol* **220** (2021).
34. Zipori, D., Friedman, A., Tamir, M., Silverberg, D. & Malik, Z. Cultured mouse marrow cell lines: interactions between fibroblastoid cells and monocytes. *J Cell Physiol* **118**, 143-152 (1984).
35. Zipori, D., Toledo, J. & von der Mark, K. Phenotypic heterogeneity among stromal cell lines from mouse bone marrow disclosed in their extracellular matrix composition and interactions with normal and leukemic cells. *Blood* **66**, 447-455 (1985).
36. Zipori, D. The nature of stem cells: state rather than entity. *Nat Rev Genet* **5**, 873-878 (2004).
37. Chaturvedi, A., Hoffman, L.M., Welm, A.L., Lessnick, S.L. & Beckerle, M.C. The EWS/FLI Oncogene Drives Changes in Cellular Morphology, Adhesion, and Migration in Ewing Sarcoma. *Genes Cancer* **3**, 102-116 (2012).
38. Bernstein, M. *et al.* Ewing's sarcoma family of tumors: current management. *Oncologist* **11**, 503-519 (2006).
39. Murphey, M.D. *et al.* From the radiologic pathology archives: ewing sarcoma family of tumors: radiologic-pathologic correlation. *Radiographics* **33**, 803-831 (2013).
40. Segal, D. *et al.* In vivo 3D profiling of site-specific human cancer cell morphotypes in zebrafish. *J Cell Biol* **221** (2022).
41. Hancock, J.D. & Lessnick, S.L. A transcriptional profiling meta-analysis reveals a core EWS-FLI gene expression signature. *Cell Cycle* **7**, 250-256 (2008).
42. Li, L., Ren, C.H., Tahir, S.A., Ren, C. & Thompson, T.C. Caveolin-1 maintains activated Akt in prostate cancer cells through scaffolding domain binding site interactions with and

inhibition of serine/threonine protein phosphatases PP1 and PP2A. *Mol Cell Biol* **23**, 9389-9404 (2003).
43. Liu, L. *et al.* Deletion of Cavin/PTRF causes global loss of caveolae, dyslipidemia, and glucose intolerance. *Cell Metab* **8**, 310-317 (2008).
44. Hill, M.M. *et al.* PTRF-Cavin, a conserved cytoplasmic protein required for caveola formation and function. *Cell* **132**, 113-124 (2008).
45. Ketteler, J. & Klein, D. Caveolin-1, cancer and therapy resistance. *Int J Cancer* **143**, 2092-2104 (2018).
46. Sheikh, E., Tran, T., Vranic, S., Levy, A. & Bonfil, R.D. Role and significance of c-KIT receptor tyrosine kinase in cancer: A review. *Bosn J Basic Med Sci* **22**, 683-698 (2022).
47. Wang, X., Bove, A.M., Simone, G. & Ma, B. Molecular Bases of VEGFR-2-Mediated Physiological Function and Pathological Role. *Front Cell Dev Biol* **8**, 599281 (2020).
48. Miao, H. *et al.* EphA2 mediates ligand-dependent inhibition and ligand-independent promotion of cell migration and invasion via a reciprocal regulatory loop with Akt. *Cancer Cell* **16**, 9-20 (2009).
49. Dagamajalu, S. *et al.* A pathway map of AXL receptor-mediated signaling network. *J Cell Commun Signal* **15**, 143-148 (2021).
50. Funamoto, S., Meili, R., Lee, S., Parry, L. & Firtel, R.A. Spatial and temporal regulation of 3-phosphoinositides by PI 3-kinase and PTEN mediates chemotaxis. *Cell* **109**, 611-623 (2002).
51. Goulden, B.D. *et al.* A high-avidity biosensor reveals plasma membrane PI(3,4)P(2) is predominantly a class I PI3K signaling product. *J Cell Biol* **218**, 1066-1079 (2019).
52. Ebner, M., Lucic, I., Leonard, T.A. & Yudushkin, I. PI(3,4,5)P(3) Engagement Restricts Akt Activity to Cellular Membranes. *Mol Cell* **65**, 416-431 e416 (2017).
53. Rocchi, A. *et al.* CD99 inhibits neural differentiation of human Ewing sarcoma cells and thereby contributes to oncogenesis. *J Clin Invest* **120**, 668-680 (2010).
54. Riggi, N. *et al.* EWS-FLI-1 expression triggers a Ewing's sarcoma initiation program in primary human mesenchymal stem cells. *Cancer Res* **68**, 2176-2185 (2008).
55. Siligan, C. *et al.* EWS-FLI1 target genes recovered from Ewing's sarcoma chromatin. *Oncogene* **24**, 2512-2524 (2005).
56. Lee, E.J., Lee, H.G., Park, S.H., Choi, E.Y. & Park, S.H. CD99 type II is a determining factor for the differentiation of primitive neuroectodermal cells. *Exp Mol Med* **35**, 438-447 (2003).
57. Singh, V. & Lamaze, C. Membrane tension buffering by caveolae: a role in cancer? *Cancer Metastasis Rev* **39**, 505-517 (2020).
58. Zundel, W., Swiersz, L.M. & Giaccia, A. Caveolin 1-mediated regulation of receptor tyrosine kinase-associated phosphatidylinositol 3-kinase activity by ceramide. *Mol Cell Biol* **20**, 1507-1514 (2000).
59. Xia, H. *et al.* Pathologic caveolin-1 regulation of PTEN in idiopathic pulmonary fibrosis. *Am J Pathol* **176**, 2626-2637 (2010).
60. Mehta, N. *et al.* Caveolin-1 regulation of Sp1 controls production of the antifibrotic protein follistatin in kidney mesangial cells. *Cell Commun Signal* **17**, 37 (2019).
61. Haugh, J.M., Codazzi, F., Teruel, M. & Meyer, T. Spatial sensing in fibroblasts mediated by 3' phosphoinositides. *J Cell Biol* **151**, 1269-1280 (2000).
62. Concordet, J.P. & Haeussler, M. CRISPOR: intuitive guide selection for CRISPR/Cas9 genome editing experiments and screens. *Nucleic Acids Res* **46**, W242-W245 (2018).
63. Lackner, D.H. *et al.* A generic strategy for CRISPR-Cas9-mediated gene tagging. *Nat Commun* **6**, 10237 (2015).

64. Shehwana, H. *et al.* RPPA SPACE: an R package for normalization and quantitation of Reverse-Phase Protein Array data. *Bioinformatics* **38**, 5131-5133 (2022).
65. Akbani, R. *et al.* A pan-cancer proteomic perspective on The Cancer Genome Atlas. *Nat Commun* **5**, 3887 (2014).
66. Siwak, D.R., Li, J., Akbani, R., Liang, H. & Lu, Y. Analytical Platforms 3: Processing Samples via the RPPA Pipeline to Generate Large-Scale Data for Clinical Studies. *Adv Exp Med Biol* **1188**, 113-147 (2019).
67. Jacques, C. *et al.* Murine Models of Bone Sarcomas. *Methods Mol Biol* **1914**, 331-342 (2019).
68. Huisken, J. & Stainier, D.Y. Even fluorescence excitation by multidirectional selective plane illumination microscopy (mSPIM). *Opt Lett* **32**, 2608-2610 (2007).
69. Chen, B. *et al.* Increasing the field-of-view in oblique plane microscopy via optical tiling. *Biomed Opt Express* **13**, 5616-5627 (2022).
70. Zhou, F.Y. *et al.* Surface-guided computing to quantify dynamic interactions between cell morphology and molecular signals in 3D. *bioRxiv*, 2023.2004.2012.536640 (2025).
71. Jaqaman, K., Galbraith, J.A., Davidson, M.W. & Galbraith, C.G. Changes in single-molecule integrin dynamics linked to local cellular behavior. *Mol Biol Cell* **27**, 1561-1569 (2016).
72. da Rocha-Azevedo, B. *et al.* Heterogeneity in VEGF Receptor-2 Mobility and Organization on the Endothelial Cell Surface Leads to Diverse Models of Activation by VEGF. *Cell Rep* **32**, 108187 (2020).
73. Driscoll, M.K. *et al.* Robust and automated detection of subcellular morphological motifs in 3D microscopy images. *Nat Methods* **16**, 1037-1044 (2019).
74. Goddard, T.D. *et al.* UCSF ChimeraX: Meeting modern challenges in visualization and analysis. *Protein Sci* **27**, 14-25 (2018).
75. Bankhead, P. *et al.* QuPath: Open source software for digital pathology image analysis. *Sci Rep* **7**, 16878 (2017).
76. Pocock, J. *et al.* TIAToolbox as an end-to-end library for advanced tissue image analytics. *Commun Med (Lond)* **2**, 120 (2022).
77. Marc Macenko , M.N., J. S. Marron, David Borland, John T. Woosley, & Xiaojun Guan , C.S., and Nancy E. Thomas A method for normalizing histology slides for quantitative analysis. *IEEE International Symposium on Biomedical Imaging: From Nano to Macro*, 1107-1110 (2009).
78. Acosta, P.H. *et al.* Intratumoral Resolution of Driver Gene Mutation Heterogeneity in Renal Cancer Using Deep Learning. *Cancer Res* **82**, 2792-2806 (2022).
79. Zhou, F.Y. *et al.* Surface-guided computing to quantify dynamic interactions between cell morphology and molecular signals in 3D. *bioRxiv*, 2023.2004.2012.536640 (2025).
80. Yu, S., Danuser, G., Zhou, Y.F in NeurIPS 2025 Worshop Imageomics (2025).

FIGURES

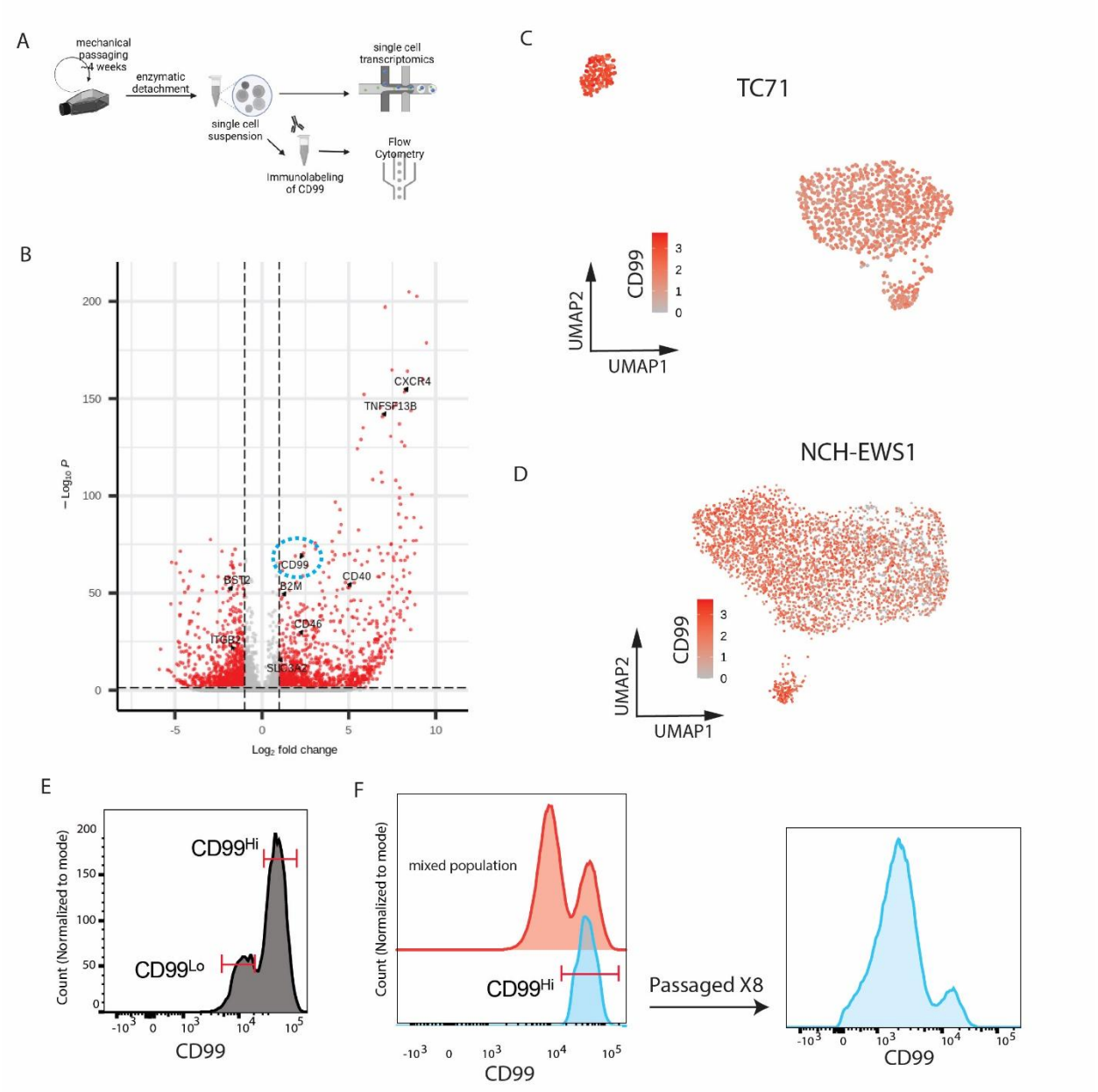

Figure 1: High levels of CD99 gene and protein expression defines a distinct Ewing Sarcoma cell state. (A) Experimental workflow. After 6-10 cycles of mechanical passaging to preserve surface receptors, cells are enzymatically detached from the dish and prepared in a cell suspension for single cell RNA seq (scRNA-seq) to profile receptor gene expression, or immunolabeling of surface-exposed receptors for flow cytometry. **(B)** Volcano plot depicting differential enrichment of transcript expression in highlighted cluster (see cluster 2 in Figure S1A) compared to all other cells. Differentially expressed cell surface receptors are indicated; CD99 is highlighted (dashed circle). **(C-D)** UMAP visualization with log normalized expression of the CD99 gene in individual cells color-coded in TC71 cells **(C)**, or in NCH-EWS1 patient-derived xenograft (PDX) cells **(D)**. **(E)** Flow cytometry histogram depicting relative intensity of cell surface exposed CD99 as measured by immunolabeling. The histogram displays a bimodal

distribution of *CD99 High* ($CD99^{Hi}$) and *CD99 Low* ($CD99^{Lo}$) cell populations. Distinct populations are highlighted by red bars. **(F)** $CD99^{HI}$ cells (blue, left) were isolated from a mixed population of $CD99^{Lo}$ and $CD99^{Hi}$ cells (red). The isolated $CD99^{Hi}$ cells were reevaluated by flow cytometry (blue, right) after expansion and several rounds of passaging. The recurrent bimodal distribution of CD99 expression suggests that $CD99^{Hi}$ cells can shift between $CD99^{Hi}$ and $CD99^{Lo}$ cell states.

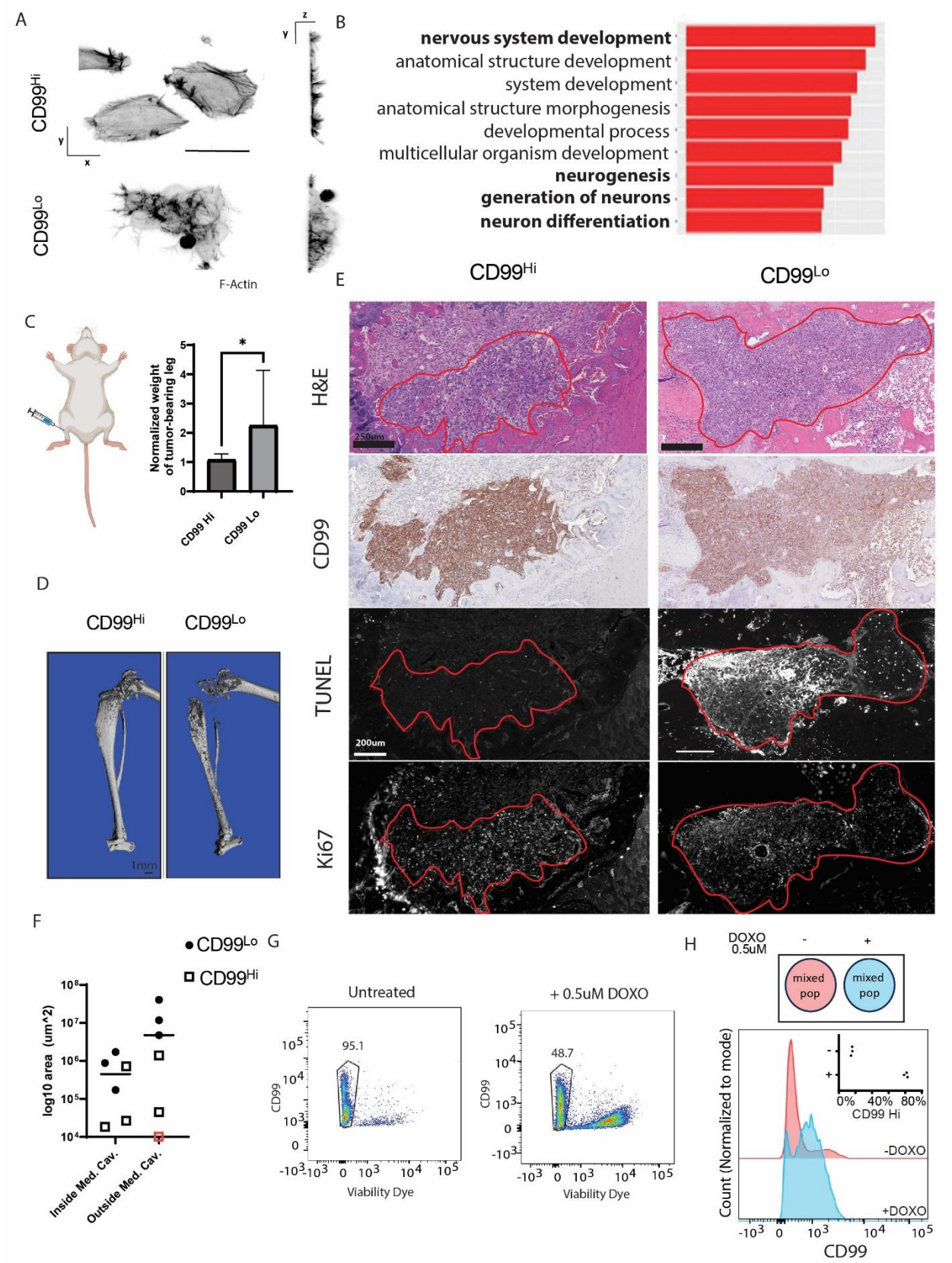
A
CD99Hi
CD99Lo
F-Actin
B
nervous system development
anatomical structure development
system development
anatomical structure morphogenesis
developmental process
multicellular organism development
neurogenesis
generation of neurons
neuron differentiation
C
Normalized weight of tumor-bearing leg
CD99 Hi
CD99 Lo
D
CD99Hi
CD99Lo
1mm
E
CD99Hi
CD99Lo
H&E
CD99
TUNEL
Ki67
250um
200um
F
CD99Lo
CD99Hi
log10 area (um^2)
Inside Med. Cav.
Outside Med. Cav.
G
Untreated
+ 0.5uM DOXO
95.1
48.7
CD99
Viability Dye
H
DOXO 0.5uM
mixed pop
mixed pop
CD99 Hi
-DOXO
+DOXO
Count (Normalized to mode)
CD99

Figure 2: CD99^{Hi} and CD99^{Lo} cells display differences in morphology, gene expression, and survival. (A) Maximum Intensity Projections in XY view (left) or YZ view (right) of CD99^{Hi} and CD99^{Lo} TC71 cells expressing F-Tractin-GFP. Cells were imaged in 3D using oblique plane microscopy in adherent culture. The two classes display distinct cell morphologies (scale bar = 20um). **(B)** Gene Ontology terms for CD99^{Hi} cells show enrichment of neurally differentiated gene signatures relative to CD99^{Lo} cells. **(C)** Schematic depicting intratibial xenografts of CD99^{Hi} or CD99^{Lo} TC71 cells into immunocompromised mice (left). Weight of tumor-bearing leg normalized to the weight of non-tumor bearing leg of the same mouse in CD99^{Hi} (n=6) or CD99^{Lo} (n=6) xenografts (right, asterisk depicts $p<0.05$, t-test). **(D)** Representative computer tomography scan of tumor bearing legs depicting less bony destruction caused by CD99^{Hi} cells compared to CD99^{Lo} cells. **(E)** Histological sections of intratibial xenografts in immunocompromised mice, showing tumor-bearing areas (outlined in red) within the medullary cavity (Med. Cav.) of either CD99^{Hi} or CD99^{Lo} cells, labeled with H&E, chemically immunostained for CD99, and fluorescently stained in serial sections for the apoptotic marker TUNEL and the proliferation marker Ki67. Note the decreased TUNEL staining observed in the CD99^{Hi} tumor compared to CD99^{Lo} tumor. **(F)** Area inside the Med. Cav. of the bone, or outside of the Med. Cav., such as within the surrounding muscle. Note that while CD99^{Lo} cells have larger clusters outside the Med. Cav., CD99^{Hi} cells have comparably smaller clusters in both areas (n = 3 mice). Red square indicates CD99^{Hi} mouse with no tumor-bearing area found outside Med. Cav. Bars, mean value. **(G)** Flow cytometry of a mixed population of CD99^{Hi} and CD99^{Lo} cells stained with Live/Dead viability dye and anti-CD99 antibody, with or without Doxorubicin treatment (DOXO, 0.5uM, 48hrs). Viable cells (Viability dye negative) constituted 95.1% of the untreated population and 48.7% of the DOXO-treated population. **(H)** Histograms depicting outlined regions from the dot plot in (G), which mark viable, CD99+ cells and show relative distributions of CD99^{Lo} and CD99^{Hi} populations grown with (+, blue) or without (-, magenta) DOXO (n=3 independent experiments). Inset, percentage enrichment of CD99^{Hi} cells in each group. CD99^{Hi} cells are systematically enriched upon drug treatment.

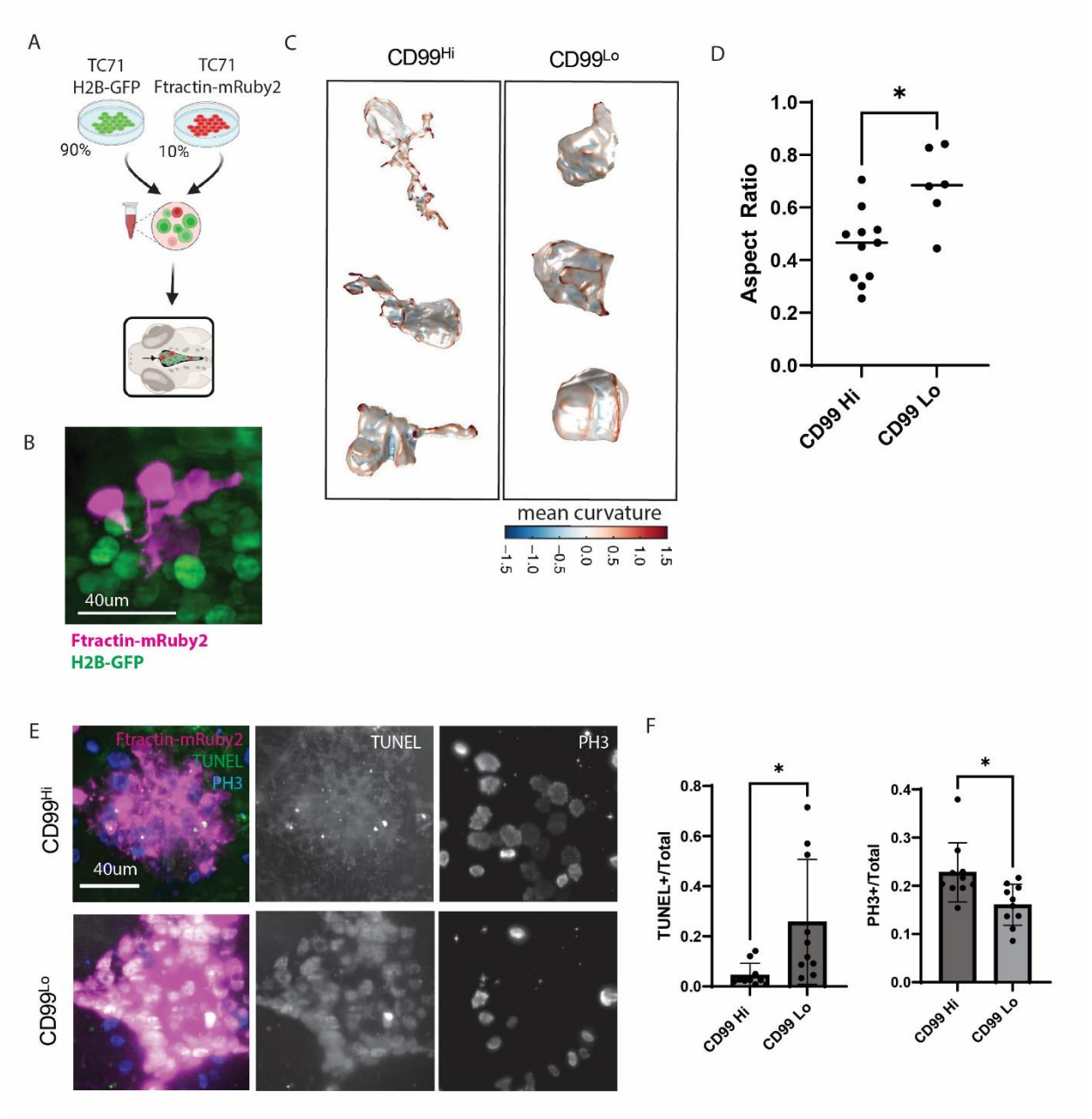

Figure 3: CD99^{Hi} and CD99^{Lo} cells display differences in morphology and survival in zebrafish xenografts. (A) Experimental set-up to identify single-cell morphologies in xenografted cells within the hindbrain ventricle (HBV) of zebrafish larvae. In order to distinguish single-cell morphologies of individual cells, we prepared a mosaic cell mixture consisting of 90% of TC71 unsorted cells expressing the fluorescently-tagged nuclear marker H2B-GFP, and 10% of TC71 CD99^{Hi} or CD99^{Lo} cells expressing F-Tractin-mRuby2. **(B)** Maximum Intensity Projection of TC71 cells within the HBV expressing F-Tractin-mRuby2 (magenta) or H2B-GFP (green). **(C)** Volume renderings of 3 representative single cells from each class, pseudocolored by local membrane curvature. Note the highly elongated and protrusive shapes observed in CD99^{Hi} cells. **(D)** Differences in aspect ratio of individual cells, as a metric of differences in cell shape in CD99^{Hi} (n = 11 cells, 9 fish) and CD99^{Lo} cells (n=6 cells, 3 fish, p-value<0.05, t-test). **(E)** TC71 CD99^{Hi} or CD99^{Lo} cells expressing F-tractin-mRuby2 (magenta) were injected into the

HBV of zebrafish larvae and stained for apoptotic marker TUNEL (green (left), grey (middle)) and proliferative marker Phospho-histone H3 (PH3, blue (left), grey (right)) 48hrs post-injection. Maximum Intensity Projections show increased TUNEL staining in CD99^{Lo} cells. **(F)** Proportion of measured area of TUNEL-positive (left) or PH3-positive (right) signal overlapping with F-Tractin-mRuby2 expressing cells (n=10 fish). Note decreased cell death and higher proliferation in CD99^{Hi} cells.

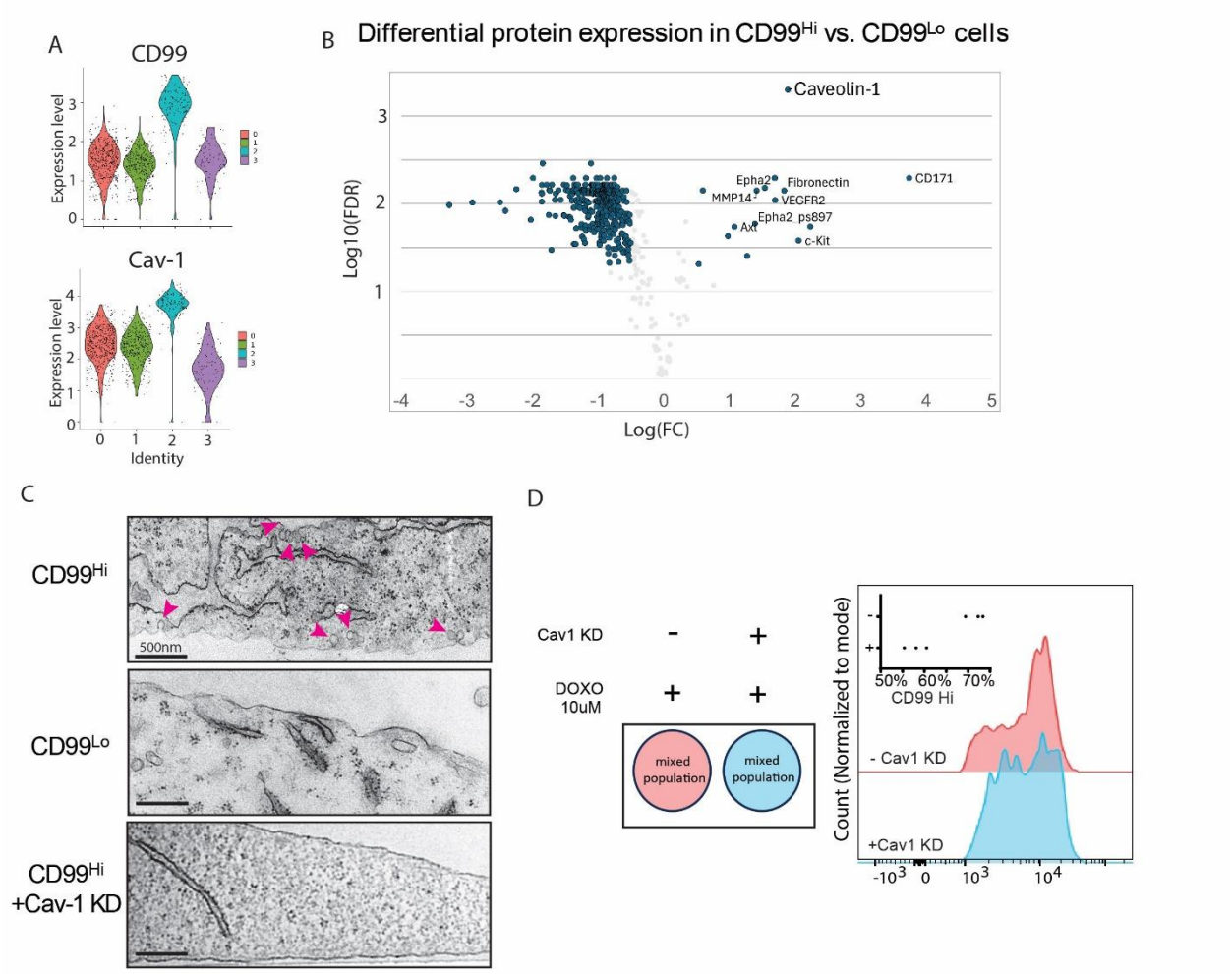

Figure 4: Caveolin-1 emerges as a potential driver of functions associated with the CD99^{Hi} State. (A) RNA expression of CD99 and Cav1 in different clusters, analyzed from scRNA-seq data (see Fig S1). **(B)** Volcano plot of differential protein expression between CD99^{Hi} vs. CD99^{Lo} cells, analyzed by Reverse Phase Protein Array (RPPA). **(C)** Representative scanning electron microscope images of CD99^{Hi}, CD99^{Lo}, and CD99^{Hi} cells expressing inducible Cav-1 shRNA (Cav1 KD). Magenta arrowheads highlight observed caveolae in CD99^{Hi} cells. **(D)** (Left) Experimental setup for a flow cytometry assay of a mixture of TC71 CD99^{Hi} and CD99^{Lo} cells, with (blue) or without (red) knockdown of Cav-1, grown with Doxorubicin (DOXO, 10uM, 48hrs). (Right) Histogram of CD99^{Hi} and CD99^{Lo} populations. Representative of n=3 experiments. Inset- percentage enrichment of CD99^{Hi} cells in each group (n=3). Note that enrichment of CD99^{Hi} peak under DOXO treatment is lost upon Cav1 KD.

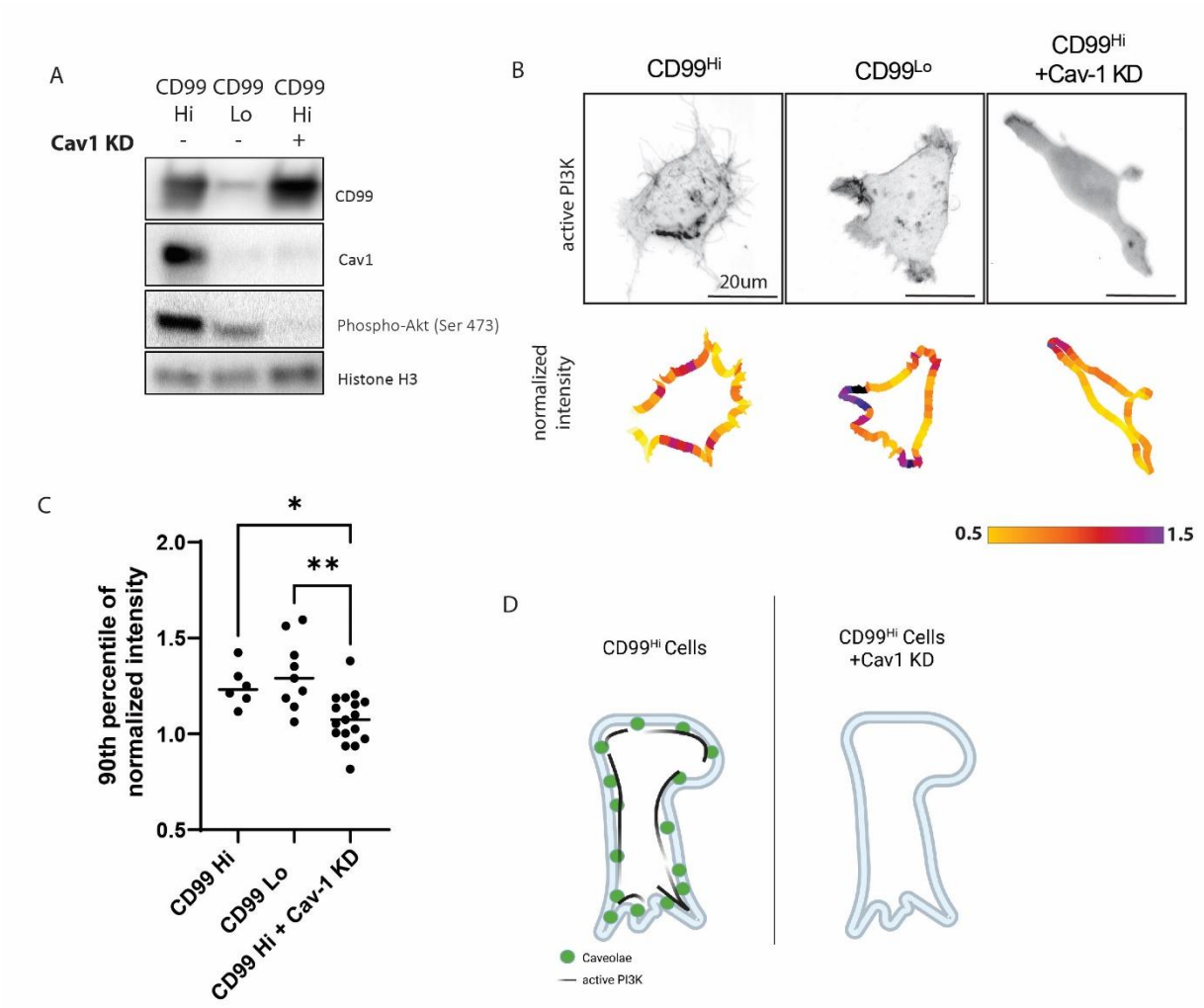

Figure 5: Caveolin-1 regulates PI3K/AKT signaling in CD99^{Hi} Cells. (A) Western blot depicting higher Cav1 expression and increased active AKT signaling in CD99^{Hi} compared to CD99^{Lo} cells, which is lost upon Cav-1 KD (n=2 independent repeats). **(B)** TC71 CD99^{Hi} and CD99^{Lo} cells, and CD99^{Hi} cells +Cav1 KD, expressing PI3K activation sensor AktPH-GFP (active PI3K). (Top) Maximum Intensity Projection, (Bottom) Measured membrane enrichment of active PI3K on cell boundary. Pseudocoloring is normalized to mean intensity of cell volume. **(C)** PI3K activity measured as 90th percentile of mean intensity on the cell surface normalized to mean intensity of cell volume (n = 6, 9, and 17 cells, for CD99^{Hi}, CD99^{Lo} cells, and CD99^{Hi} + Cav1 KD, respectively. (* p-value <0.05,** p-value<0.001, KS test). **(D)** Summary of proposed mechanism. CD99^{Hi} express high levels of Cav-1 and contain abundant caveolae, which alter membrane properties to stabilize active PI3K at the cell surface and promote downstream signaling. In contrast, CD99^{Hi} cells with reduced Cav-1 expression lack caveolae, resulting in impaired recruitment of active PI3K to the membrane and failure of signaling.